LAWRENCE
LIVERMORE
NATIONAL
LABORATORY

UCRL-CONF-212026

Implicit Solution of Non-Equilibrium Radiation Diffusion Including Reactive Heating Source in Material Energy Equation

D. E. Shumaker, C. S. Woodward

May 6, 2005

Computational Methods in Transport Workshop
Tahoe City, CA, United States
September 15, 2004 through September 17, 2004

Disclaimer

This document was prepared as an account of work sponsored by an agency of the United States Government. Neither the United States Government nor the University of California nor any of their employees, makes any warranty, express or implied, or assumes any legal liability or responsibility for the accuracy, completeness, or usefulness of any information, apparatus, product, or process disclosed, or represents that its use would not infringe privately owned rights. Reference herein to any specific commercial product, process, or service by trade name, trademark, manufacturer, or otherwise, does not necessarily constitute or imply its endorsement, recommendation, or favoring by the United States Government or the University of California. The views and opinions of authors expressed herein do not necessarily state or reflect those of the United States Government or the University of California, and shall not be used for advertising or product endorsement purposes.

Implicit Solution of Non-Equilibrium Radiation Diffusion Including Reactive Heating Source in Material Energy Equation

Dana E. Shumaker[1] and Carol S. Woodward[2]

[1] Lawrence Livermore National Laboratory shumaker1@llnl.gov
[2] Lawrence Livermore National Laboratory cswoodward@llnl.gov

1 Introduction

In this paper, we investigate performance of a fully implicit formulation and solution method of a diffusion-reaction system modeling radiation diffusion with material energy transfer and a fusion fuel source. In certain parameter regimes this system can lead to a rapid conversion of potential energy into material energy. Accuracy in time integration is essential for a good solution since a major fraction of the fuel can be depleted in a very short time. Such systems arise in a number of application areas including evolution of a star [1] and inertial confinement fusion [2].

Previous work has addressed implicit solution of radiation diffusion problems [3, 4, 5, 6, 7, 8]. Recently Shadid and coauthors have looked at implicit and semi-implicit solution of reaction-diffusion systems. In general they have found that fully implicit is the most accurate method for difficult coupled nonlinear equations [9, 10]. In previous work, we have demonstrated that a method of lines approach coupled with a BDF time integrator and a Newton-Krylov nonlinear solver could efficiently and accurately solve a large-scale, implicit radiation diffusion problem [7, 8]. In this paper, we extend that work to include an additional heating term in the material energy equation and an equation to model the evolution of the reactive fuel density. This system now consists of three coupled equations for radiation energy, material energy, and fuel density. The radiation energy equation includes diffusion and energy exchange with material energy. The material energy equation includes reaction heating and exchange with radiation energy, and the fuel density equation includes its depletion due to the fuel consumption.

In many applications, the added heat source involves a reaction rate with a strong nonlinear dependence on material temperature and thus provides a good test for an implicit solution method. We use an approximation to the reaction rate valid for temperature regimes less than 1 keV where the rate has its strongest dependence on material temperature. In particular, the rate

depends on temperature to the fifth power in this regime. While the actual reaction rate drops off at high temperature, we use the the fifth power fit for any temperature in order to investigate the performance of implicit solution techniques on problems with strong nonlinearities.

The remainder of this paper is organized as follows. The next section describes the model and presents the equations we are solving. Section 3 describes the implicit solution method we employ, and Section 4 presents numerical results illustrating accuracy and efficiency of the solution method. Conclusions are presented in the last section.

2 Model

We consider a flux-limited formulation of radiation diffusion including a model for heating due to a fusion source term. The evolution of the fusion fuel density is determined by an equation which models the depletion of the fuel as its fusion energy is added to the material energy.

The radiation diffusion model is given by [11, 12]

$$\frac{\partial E_R}{\partial t} = \nabla \cdot \left(\frac{c}{3\rho\kappa_R(T_R) + \frac{\|\nabla E_R\|}{E_R}} \nabla E_R \right) + c\rho\kappa_P(T_M) \cdot \left(aT_M^4 - E_R \right), \quad (1)$$

where $E_R(\mathbf{x}, t)$ is the radiation energy density ($\mathbf{x} = (x, y, z)$), $T_M(\mathbf{x}, t)$ is the material temperature, $\rho(\mathbf{x})$ is the material density, c is the speed of light, and $a = 4\sigma/c$ where σ is the Stephan–Boltzmann constant. The Rosseland opacity, κ_R, is a nonlinear function of the radiation temperature, T_R, which is defined by the relation $E_R = aT_R^4$. The Planck opacity, κ_P, is a nonlinear function of material temperature, T_M, which is related to the material energy through an equation of state, $E_M = \mathrm{EOS}(T_M)$. In this paper, when we take variable opacity and specific heat their values are taken from the LEOS equation-of-state package [13] which determines opacities and specific heats via table look-up. In some simplified test problems we use the relation, $E_M = \rho c_v T_M$, for the specific heat and constant values for opacities. In the flux limiter, the norm $\|\cdot\|$ is taken to be the l^2 norm of the gradient vector. In the simulations presented here we use either Dirichlet or Neumann boundary conditions on the radiation energy.

This equation is solved in conjunction with two other equations, one being the conservation of material energy [11, 12] given by

$$\frac{\partial E_M}{\partial t} = -c\rho\kappa_P(T_M) \cdot \left(aT_M^4 - E_R \right) + e_r \sigma_v {\rho_F}^2 \left(\frac{T_M}{T_0} \right)^5. \quad (2)$$

The heating term is controlled by a fusion model [14](p. 13) of fuel density given by

$$\frac{\partial \rho_F}{\partial t} = -\sigma_v {\rho_F}^2 \left(\frac{T_M}{T_0} \right)^5, \quad (3)$$

where ρ_F is the fuel density. This evolution equation has been used in controlled fusion models [15](p. 322).

The fit to the reaction rate gives, $\sigma_v = 1.43 \times 10^3 \frac{cm^3}{sec-g}$, with a reference temperature, T_0, of 1 keV. For the energy per reaction we use, $e_r = 1.35 \times 10^{18} \frac{erg}{sec-g}$. This value corresponds to the alpha particle energy from deuterium tritium fusion. We neglect the neutron energy from the reaction and assume the alpha particle has zero range, thus depositing its energy locally.

Both the material energy and the fuel density equations contain the nonlinear temperature dependence term $(T_M/T_0)^5$. This dependency is a good fit to a tritium-deuterium reaction rate at low temperature (less than a few keV) such as in a tokamak fusion experiment [16] (p. 29). The reference temperature, T_0, is a normalization constant (1 keV) included to simplify the units of the fitted reaction rate σ_v. The actual reaction is less strongly dependent on T_M above 1 keV, but, as noted above, we will use this approximation above that temperature.

The fusion fuel is assumed to be a 50:50 mixture of tritium and deuterium with ρ_F representing the tritium or deuterium density. The binary nature of the reaction leads to the ${\rho_F}^2$ dependence in the reaction rate. The energy per reaction added to the material energy equation is e_r.

Obviously there are a significant number of physical processes omitted from this simple model. One relevant to the deposition of heat, is that we assume the energy of reaction is deposited locally. The correct physical process would distribute the heat spatially due to the finite range of the charged particles in the matter. We chose not to model this nonlocal effect here.

3 Numerical Methods

In this section we present both the spatial and temporal discretization methods used for solution of the system (1)-(3).

3.1 Spatial Discretization

For spatial discretization, we employ a cell-centered finite difference scheme. We use a tensor product grid with N_x, N_y, and N_z cells in the x, y, and z directions, respectively. Defining $E_{R,i,j,k}(t) \approx E_R(\mathbf{x}_{i,j,k}, t)$, $E_{M,i,j,k}(t) \approx E_M(\mathbf{x}_{i,j,k}, t)$, and $\rho_{F,i,j,k}(t) \approx \rho_F(\mathbf{x}_{i,j,k}, t)$ with $\mathbf{x}_{i,j,k} = (x_i, y_j, z_k)$, and

$$\mathbf{E_R} \equiv \begin{pmatrix} E_{R,1,1,1} \\ \vdots \\ E_{R,N_x,N_y,N_z} \end{pmatrix} \mathbf{E_M} \equiv \begin{pmatrix} E_{M,1,1,1} \\ \vdots \\ E_{M,N_x,N_y,N_z} \end{pmatrix} \rho_\mathbf{F} \equiv \begin{pmatrix} \rho_{F,1,1,1} \\ \vdots \\ \rho_{F,N_x,N_y,N_z} \end{pmatrix},$$

we can write our discrete equations in terms of a discrete diffusion operator given by

$$\mathbf{L}(\mathbf{E_R}) \equiv \left(L_{1,1,1}(\mathbf{E_R}), \cdots, L_{N_x,N_y,N_z}(\mathbf{E_R})\right)^T, \tag{4}$$

a local coupling operator given by

$$\mathbf{S}(\mathbf{E_R}, \mathbf{E_M}) \equiv (S_{1,1,1}(\mathbf{E_R}, \mathbf{E_M}), \cdots, S_{N_x,N_y,N_z}(\mathbf{E_R}, \mathbf{E_M}))^T, \tag{5}$$

and the local reaction rate operator given by

$$\mathbf{R}(\mathbf{E_M}, \rho_\mathbf{F}) \equiv (R_{1,1,1}(\mathbf{E_M}, \rho_\mathbf{F}), \cdots, R_{N_x,N_y,N_z}(\mathbf{E_M}, \rho_\mathbf{F}))^T, \tag{6}$$

where, as in [8]

$$\begin{aligned} &L_{i,j,k}(\mathbf{E_R}) \equiv \\ &\left(D_{i+1/2,j,k}\frac{E_{R,i+1,j,k} - E_{R,i,j,k}}{\Delta x_{i+1/2,j,k}} - D_{i-1/2,j,k}\frac{E_{R,i,j,k} - E_{R,i-1,j,k}}{\Delta x_{i-1/2,j,k}}\right)/\Delta x_i \\ &+ \left(D_{i,j+1/2,k}\frac{E_{R,i,j+1,k} - E_{R,i,j,k}}{\Delta y_{i,j+1/2,k}} - D_{i,j-1/2,k}\frac{E_{R,i,j,k} - E_{R,i,j-1,k}}{\Delta y_{i,j-1/2,k}}\right)/\Delta y_j \\ &+ \left(D_{i,j,k+1/2}\frac{E_{R,i,j,k+1} - E_{R,i,j,k}}{\Delta z_{i,j,k+1/2}} - D_{i,j,k-1/2}\frac{E_{R,i,j,k} - E_{R,i,j,k-1}}{\Delta z_{i,j,k-1/2}}\right)/\Delta z_k \end{aligned} \tag{7}$$

with the diffusion coefficients evaluated on the face centers,

$$\begin{aligned} D_{i+1/2,j,k} &\equiv \frac{c}{3\rho_{i+1/2,j,k}\kappa_{R,i+1/2,j,k} + \|\nabla E_R\|_{i+1/2,j,k}/E_{R,i+1/2,j,k}}, \\ D_{i-1/2,j,k} &\equiv \frac{c}{3\rho_{i-1/2,j,k}\kappa_{R,i-1/2,j,k} + \|\nabla E_R\|_{i-1/2,j,k}/E_{R,i-1/2,j,k}}, \end{aligned}$$

with y and z terms similarly defined,

$$S_{i,j,k}(E_{R,i,j,k}, E_{M,i,j,k}) = c\rho_{i,j,k}\kappa_{P,i,j,k}\left(aT^4_{M,i,j,k} - E_{R,i,j,k}\right). \tag{8}$$

and

$$R_{i,j,k}(E_{M,i,j,k}, \rho_{F,i,j,k}) = \sigma_v \rho^2_{F,i,j,k}\left(\frac{T_{M,i,j,k}}{T_0}\right)^5. \tag{9}$$

Thus, our discrete scheme is to find $\mathbf{E_R}(t)$ and $\mathbf{E_M}(t)$ such that,

$$\frac{d\mathbf{E_R}}{dt} = \mathbf{L}(\mathbf{E_R}) + \mathbf{S}(\mathbf{E_R}, \mathbf{E_M}), \tag{10}$$

$$\frac{d\mathbf{E_M}}{dt} = -\mathbf{S}(\mathbf{E_R}, \mathbf{E_M}) + e_r\mathbf{R}(\mathbf{E_M}, \rho_\mathbf{F}), \tag{11}$$

$$\frac{d\rho_\mathbf{F}}{dt} = -\mathbf{R}(\mathbf{E_M}, \rho_\mathbf{F}). \tag{12}$$

For more details, see [8, 7].

3.2 Time Integration

We formulate (10)-(12) as an implicit system of ordinary differential equations (ODEs) and use an ODE time integrator to handle the implicit time step selection. In particular, we employ the parallel ODE solver, CVODE [17], developed at Lawrence Livermore National Laboratory and included in the SUNDIALS package [18]. CVODE employs the fixed leading coefficient variant of the Backward Differentiation Formula (BDF) method [19, 20] and allows for variation in the order of the time discretization as well as in the time step size. Time step sizes are chosen to minimize the local truncation error and thus give a solution that obeys a user-specified accuracy bound.

This time integration technique leads to a coupled, nonlinear system of equations that must be solved at each time step. For example, solving the ODE system

$$\dot{y} = f(t, y), \tag{13}$$

with the backward Euler method leads to the following nonlinear system

$$\frac{y_n - y_{n-1}}{\Delta t} = f(t_n, y_n) \tag{14}$$

that must be solved at each time step. For the solution of this system, we use an inexact Newton–Krylov method with Jacobian-vector products approximated by finite differences. As the methods in CVODE are predictor-corrector in nature, an explicit predictor (e.g., forward Euler in the case above) is used for an initial guess in the nonlinear solve.

In the methods discussed above, we use the scaling technique incorporated into CVODE. Thus, we include an absolute tolerance (ATOL) for each unknown and a relative tolerance (RTOL) which is applied to all unknowns. These tolerances are then used to form a weight which is applied to each solution component during the time step from t_{n-1} to t_n. This weight is given as

$$w_i = RTOL|y_{n-1}^i| + ATOL_i \tag{15}$$

and is also used to weight a root mean square norm

$$\|y\|_{WRMS} = \left[N^{-1} \sum_{1}^{N} (y_i/w_i)^2 \right]^{1/2} \tag{16}$$

which is applied to all error-like vectors within the solution process.

We use the GMRES Krylov iterative solver for solution of the linear Jacobian system at each Newton iteration [21]. The tolerance for the Newton iteration is taken to guarantee that iteration error introduced from the nonlinear solver is smaller than the local truncation error. For more details regarding the step size and order selection strategies in CVODE, as well as acceptance of a step and nonlinear convergence, we refer the reader to the review article [18].

3.3 Preconditioning

Preconditioning is generally essential when using Krylov linear solvers. To describe our preconditioning strategy, we begin by considering the content and structure of the Jacobian matrix. In (13), set $y = (\mathbf{E_R}^T, \mathbf{E_M}^T, {\rho_F}^T)^T$, and then form f using the right-hand sides of (10)-(12). The Jacobian matrices used in the Newton method are of the general form $F'(y) = (I - \gamma J)$, where $J = \partial f/\partial y$ is the Jacobian of the nonlinear function f, and the parameter $\gamma \equiv \Delta t\beta$ with Δt the current time step value and β a coefficient depending on the order of the BDF method. Recalling the definitions of the discrete divergence, coupling and reaction rate operators, the block form of the Jacobian of f is

$$J = \begin{pmatrix} \partial\mathbf{L}/\partial\mathbf{E_R} + \partial\mathbf{S}/\partial\mathbf{E_R} & \partial\mathbf{S}/\partial\mathbf{E_M} & 0 \\ -\partial\mathbf{S}/\partial\mathbf{E_R} & -\partial\mathbf{S}/\partial\mathbf{E_M} + e_r\partial\mathbf{R}/\partial\mathbf{E_M} & e_r\,\partial\mathbf{R}/\partial\rho_\mathbf{F} \\ 0 & -\partial\mathbf{R}/\partial\mathbf{E_M} & -\partial\mathbf{R}/\partial\rho_\mathbf{F} \end{pmatrix}$$
$$= \begin{pmatrix} A+G & B & 0 \\ -G & -B+e_rC & e_rH \\ 0 & -C & -H \end{pmatrix},$$

where $A = \partial\mathbf{L}/\partial\mathbf{E_R}$, $G = \partial\mathbf{S}/\partial\mathbf{E_R}$, $B = \partial\mathbf{S}/\partial\mathbf{E_M}$, $C = \partial\mathbf{R}/\partial\mathbf{E_M}$, and $H = \partial\mathbf{R}/\partial\rho_\mathbf{F}$. We note that G, B, C and H are diagonal matrices. In all of our preconditioning strategies, we neglect the nonlinearity in the diffusion term and use the approximation [8, 7]

$$A = \partial\mathbf{L}(\hat{\mathbf{E}}_R)/\partial\mathbf{E_R} \approx \hat{\mathbf{L}}(\hat{\mathbf{E}}_R) \equiv \tilde{A},$$

where $\partial\mathbf{L}(\hat{\mathbf{E}}_R)/\partial\mathbf{E_R}$ is the Jacobian of $\mathbf{L}$ evaluated at a radiation energy, $\hat{\mathbf{E}}_R$. The size of the neglected term is related to the derivatives of the Rosseland opacity and the flux-limiter. Our motivation for neglecting this term arises from the fact that $-\tilde{A}$ is symmetric and positive definite, whereas $-A$ is not, and we thus can use multigrid methods for solution of diffusion terms within the preconditioner.

Our preconditioning strategy is to factor the matrix, $M \equiv I - \gamma\tilde{J}$, as

$$\begin{pmatrix} P & Q & 0 \\ U & T & V \\ 0 & Y & Z \end{pmatrix} \equiv \begin{pmatrix} I-\gamma(\tilde{A}+G) & -\gamma B & 0 \\ \gamma G & I-\gamma(e_rC-B) & -\gamma e_rH \\ 0 & \gamma C & I+\gamma H \end{pmatrix} = M$$

The preconditioner solve then consists of solving $M_{Schur}x = b$ for x where,

$$M_{Schur} = \begin{pmatrix} I & Q\tilde{T}^{-1} & 0 \\ 0 & I & VZ^{-1} \\ 0 & 0 & I \end{pmatrix} \begin{pmatrix} S & 0 & 0 \\ 0 & \tilde{T} & 0 \\ 0 & 0 & Z \end{pmatrix} \begin{pmatrix} I & 0 & 0 \\ \tilde{T}^{-1}U & I & 0 \\ 0 & Z^{-1}Y & I \end{pmatrix} \qquad (17)$$

with $S = P - Q\tilde{T}^{-1}U$ and $\tilde{T} = T - VZ^{-1}Y$. Thus,

$$\begin{pmatrix} x_1 \\ x_2 \\ x_3 \end{pmatrix} = \begin{pmatrix} S^{-1}(b_1 - Q\tilde{T}^{-1}\tilde{b_2}) \\ \tilde{T}^{-1}(\tilde{b_2} - Ux_1) \\ Z^{-1}(b_3 - Yx_2) \end{pmatrix} \tag{18}$$

where $\tilde{b_2} = b_2 - VZ^{-1}b_3$.

If the Schur complement, S, is exactly inverted, there will be no error associated with this preconditioner for the non-flux-limited, constant opacity case. In addition, because G, B, C, H and hence $\tilde{T}$ and Z are diagonal, there is no penalty associated with inverting $\tilde{T}$ for every iteration of a method that inverts S. Also note that S is formed by modifying the diagonal of P and thus is composed of a symmetric diffusion-like matrix with a modified diagonal. Hence, we can employ multigrid methods to invert this Schur complement.

Dependence of opacities on temperatures can give rise to large spatial gradients and thus a very heterogeneous problem. Hence, to invert the Schur complement matrix, S, we use a multigrid method designed to handle large changes in problem coefficients. In particular, we use one V-cycle of a semi-coarsening multigrid algorithm, such as the ParFlow semi-coarsening Multi-Grid (PFMG)[22] or the Semi-coarsening MultiGrid (SMG) developed by Schaffer [23, 24] as our multigrid solver. Semi-coarsening multigrid methods have been found to be quite effective on highly heterogeneous problems. A comparison of PFMG and SMG can be found in [25]. Details of both these methods can be found in the cited references, and more information about multigrid methods in general can be found in [26].

4 Results

In this section we demonstrate the above solution method on the implicit formulation of (1)-(3). In the first two subsections we present illustrations of problems modeled by this system of equations. In the next two subsections we give results which verify the accuracy and convergence of the method.

4.1 1D Solution Illustration

In this section we illustrate how the time evolution of the solution is affected by the initial fuel density. This 1D problem has a domain from 0 cm to 10.0 cm. The fuel is initialized using a step function with fuel density, ρ_{F0}, on the left half of the domain and 0 on the right. The initial radiation and material temperatures are equal and constant in the domain. Neumann boundary conditions are applied on the left boundary, $\frac{\partial E_R}{\partial x} = 0$, while Dirichlet boundary conditions are applied on the right boundary with the temperature set to the initial value.

Results are presented for two different initial conditions; one with a high fuel density, and the other with a low fuel density. The high density simulation has ρ_{F0} of 0.03 g/cm^3 and $T_R = T_M$ of 0.5 keV. The low density simulation

uses $\rho_{F0} = 0.01\ g/cm^3$ and $T_R = T_M = 0.776\ keV$. These initial temperatures were selected so that the initial heating rates, $\rho_F^2\ T_M^5$, are approximately the same for both simulations.

Fig. 1 illustrates the evolution of the radiation and material temperature, as well as fuel density of a point near the left boundary. As can be seen, the high density case yields a very rapid increase in material temperature and consumes most of the fuel. The low density case results in a slower evolution of the material temperature. The slowly changing temperature allows for more energy to be transfered to the radiation and loss via diffusion. Since the temperature is lower in this case, a smaller fraction of the fuel is consumed.

Fig. 2 shows profiles of radiation temperature, material temperature, and fuel density at various times for the $\rho_{F0} = 0.03\ g/cm^3$ simulation. Diffusion loss of energy results in a lower temperature in the outer region. Thus, the inner region begins to consume fuel and heat up sooner than the outer region resulting in a steep temperature gradient that sweeps through the fuel region (see Fig. 2). These results are similar to the reaction-diffusion wave results presented in the next section.

Fig. 3 gives the history of the time step and integration order for the higher fuel density case. The smallest step size, which occurs during the rapid heating stage, is $3.26 \times 10^{-8} \mu s$. The longest time, in the quiescent period at the end of the simulation, is $5.31 \times 10^{-4} \mu s$. This large difference in step sizes illustrates the ability of our method to select time step size and integration order resulting in the largest time step possible subject to the accuracy constraints.

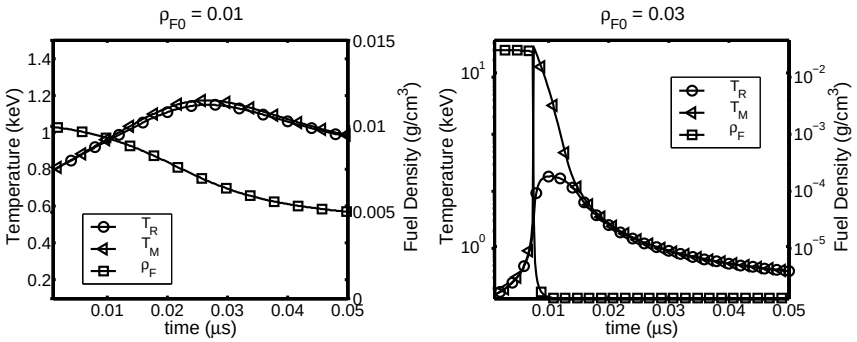

Fig. 1. Evolution of radiation temperature, material temperature, and fuel density for two simulations. Values plotted are for a point near the left boundary. Linear scale used on the low density case and a log scale used on the high density case.

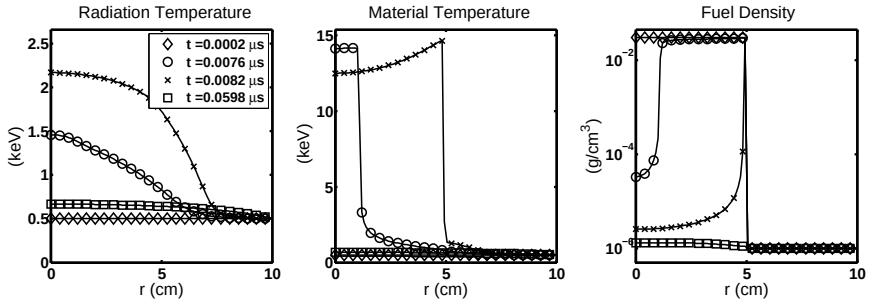

Fig. 2. Radiation temperature, material temperature and fuel density profiles at various times for the $\rho_{F0} = 0.03\ g/cm^3$ run.

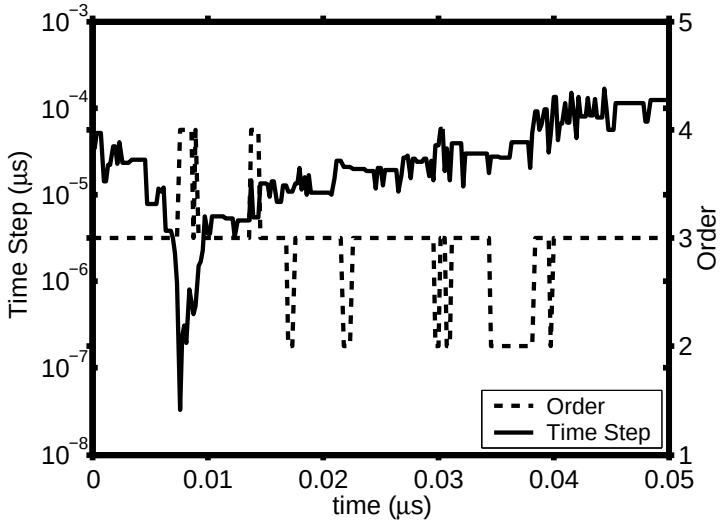

Fig. 3. History of time step and integration order.

4.2 1D Reaction Diffusion Wave

In the previous section we initialized the simulation with a uniform initial material temperature and a step function for the initial fuel density. The simulation in this section begins with a uniform fuel density and a step function in the initial material temperature. These initial conditions produce a reaction diffusion wave which is propagated by the diffusion of radiation energy and is driven by the energy from the fusion reaction.

The 1D domain for this simulation is 0.0 to 2.0 cm, with a uniform fuel density of 0.1 g/cm^3, and uses 200 grid points. The initial background radiation and material temperatures are set to 0.1 keV except for a small region on

the left from 0 to 0.1 cm where the material energy is initilized to 2.0 keV. The reaction parameters are, $\sigma_v = 1.43 \times 10^3 \frac{cm^3}{sec-g}$ and $e_r = 1.35 \times 10^{18} \frac{erg}{sec-g}$. This simulation also uses the LEOS equation-of-state data base [13] for hydrogen.

The high density region begins to heat much faster than the remainder of the domain. Diffusion of radiation energy heats the material in front of the wave leading to more heating due to the fusion reactions. Fig. 4 gives profiles at four different times.

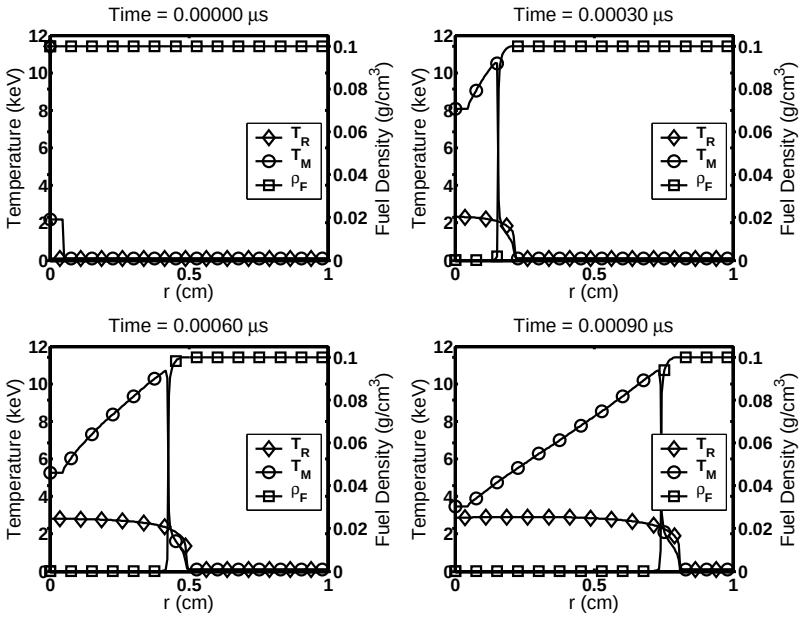

Fig. 4. Profiles at various times for a reaction diffusion wave moving from left to right.

4.3 0D Analytic Test

In this section we demonstrate accuracy of the implicit solution for fusion heating of the material and the fuel evolution by a comparison with an analytic solution.

In order to obtain the analytic results, two simplifying assumptions are made. First, we assume $\kappa_P = 0$. This assumption eliminates the exchange of energy between radiation and material and thus removes the radiation energy equation and diffusion from the system. With this assumption the material energy equation reduces to,

$$\frac{\partial E_M}{\partial t} = e_r \sigma_v {\rho_F}^2 \left(\frac{T_M}{T_0}\right)^5. \tag{19}$$

Second, the relationship between E_M and T_M, normally determined by tables in LEOS, is replaced by the simple linear relation, $E_M = \rho c_v T_M$, where the specific heat, c_v, is assumed to be a constant.

From the coupled pair of equations (19) and (3), it can be shown that the sum of the material energy, E_M, and the potential nuclear energy, $e_r \rho_F$,

$$W = E_M + e_r \rho_F, \tag{20}$$

is independent of time. Thus we can use the conservation relation,

$$E_M(t) + e_r \rho_F(t) = E_{M0} + e_r \rho_{F0}, \tag{21}$$

to eliminate $E_M(t)$ from (3), which becomes,

$$\frac{\partial \rho_F}{\partial \tau} = -\rho_F^2(\tau) \left(b - \rho_F(\tau)\right)^5, \tag{22}$$

where $b = E_{M0}/e_r + \rho_{F0}$ and $\tau = \sigma_v \left(\frac{e_r}{\rho c_v T_0}\right)^5 t$, and where the initial fuel density and material energy are ρ_{F0} and E_{M0}, respectively.

With some help from *Mathematica* the solution can be expressed as a transcendental equation,

$$L(\rho_{F0}) + P(\rho_{F0}) - L(\rho_F(\tau)) - P(\rho_F(\tau)) = \tau, \tag{23}$$

where L and P are given by,

$$L(\rho_F(\tau)) = \frac{5}{b^6} \left(log(\rho_F(\tau)) - log(\rho_F(\tau) - b)\right), \tag{24}$$

and,

$$P(\rho_F(\tau)) = \frac{-4b^4 + \frac{500}{12} b^3 \rho_F(\tau) - \frac{260}{3} b^2 \rho_F^2(\tau) + 70 b \rho_F^3(\tau) - 20 \rho_F^4(\tau)}{4b^5 \left(b - \rho_F(\tau)\right)^4 \rho_F(\tau)}. \tag{25}$$

This analytic result can be used in two different ways. We could solve the transcendental equation (23) for $\rho_F(\tau)$ at a number of different times, τ, then compare these values with the computed solution from our code. Or, we could use equation (23) to solve for τ when $\rho_F(\tau)$ is some fraction, α, of the initial value, $\rho_F(0)$. We chose the latter method, since it avoids any computation error associated with a transcendental solution. The time at which $\rho_F(\tau) = \alpha \rho_{F0}$ is obtained from (23),

$$\tau_\alpha = L(\rho_{F0}) + P(\rho_{F0}) - L(\alpha \rho_{F0}) - P(\alpha \rho_{F0}) \tag{26}$$

The τ, and thus t, determined by the above equation, is used to verify our solution. After we have established the parameters for a test run and

selected a value for α, we use this equation to determine a stopping time for the simulation. The simulation computes the final fuel density, and this density is then compared to the expected $\alpha\rho_{F0}$.

For this test problem we use the following parameters, $\rho = 1.0\ g/cm^3$, $c_v = 5.755 \times 10^{14}\ erg/keV$, $e_r = 1.35 \times 10^6 \frac{erg}{sec-g}$, and $\sigma_v = 1.43 \times 10^3\ \frac{cm^3}{sec-g}$. The initial material temperature is $50.0\ keV$, and the initial fuel density is $0.1\ g/cm^3$. We chose three values of α, (0.5, 0.1 and 0.01), to determine check point times. These times are indicated on Fig. 5 which gives the fuel density versus time for this simulation.

Table 1 gives the relative error in fuel density for values of RTOL from 10^{-4} to 10^{-12} along with the number of time steps, NST. We see that the error decreases linearly with the RTOL value indicating good convergence of the implicit solution method. We also see a fairly large increase in the number of time steps required to resolve the solution for RTOL values less than 10^{-8}. As one would expect, requiring very high accuracy comes at a price in computation time.

Table 1. Statistics and Error for 0D Analytic Problem

	$\rho_F = 0.5\rho_F(0)$		$\rho_F = 0.1\rho_F(0)$		$\rho_F = 0.1\rho_F(0)$	
RTOL	NST	ERROR	NST	ERROR	NST	ERROR
10^{-4}	144	-1.01×10^{-2}	159	-2.09×10^{-2}	196	-1.74×10^{-3}
10^{-6}	157	-1.65×10^{-3}	177	-3.08×10^{-3}	219	-4.81×10^{-4}
10^{-8}	173	-2.79×10^{-5}	217	-5.18×10^{-5}	289	-4.51×10^{-6}
10^{-10}	258	-2.93×10^{-7}	359	-5.67×10^{-7}	500	4.72×10^{-9}
10^{-12}	484	-9.84×10^{-9}	686	-1.72×10^{-8}	967	-1.87×10^{-10}

4.4 2D Results

In this section we present results for a 2D problem illustrating the convergence with respect to reducing tolerances and varying the maximum allowed order of integration. The simulation domain consists of a square region $1cm$ by $1cm$ with 50 grid points in each direction. The initial fuel density is centered at x=y=0.0 with a smooth radial distribution given by,

$$\rho_F(\mathbf{x}) = 0.1\ B\left(\sqrt{x^2+y^2}, 0.75\right)(g/cm^3), \tag{27}$$

where the bicubic radial distribution, $B(x,\epsilon)$, is given by,

$$B(x,\epsilon) \equiv \begin{cases} 2\left(\frac{\epsilon+x}{2\epsilon}\right)^2\left(6 - 8\frac{\epsilon+x}{2\epsilon}\right), & \text{if } -\epsilon < x \le 0; \\ 2\left(\frac{\epsilon-x}{2\epsilon}\right)^2\left(6 - 8\frac{\epsilon-x}{2\epsilon}\right), & \text{if } 0 \le x < \epsilon; \\ 0, & \text{otherwise.} \end{cases} \cdot \tag{28}$$

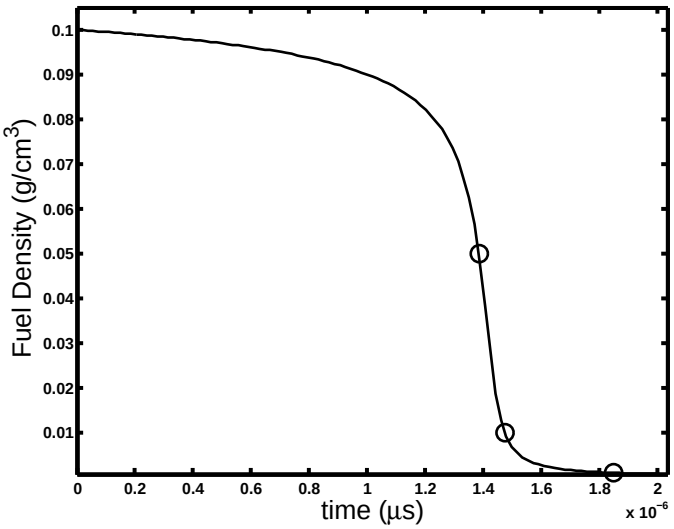

Fig. 5. Evolution of fuel density for 0D analytic comparison test problem. Markers indicate the compared test values at $\rho_F = 0.5\rho_F(0)$, $\rho_F = 0.1\rho_F(0)$ and $\rho_F = 0.01\rho_F(0)$.

This simulation uses the LEOS equation-of-state data base [13] for hydrogen which has a uniform density of $5.0\,g/cm^3$. Neumann boundary conditions are applied at the $x = 0$ and $y = 0$ boundaries. Dirichlet boundary conditions are applied at $x = 1$ and $y = 1$ where radiation temperature is set to $0.5\ keV$. Radiation and material temperatures were also set to this value. For this simulation, the energy per reaction, e_r, is set to $1.35 \times 10^{18} \frac{erg}{sec-g}$. The reaction rate fit parameter, σ_v, is $1.43 \times 10^3\ \frac{cm^3}{sec-g}$ as determined for plots in [16]. The reference temperature, T_0, is $1\ keV$.

Fig. 6 gives the time histories of material and radiation temperatures and fuel density for the point $x = 0, y = 0$. The material temperature rises slowly initially; however, the T_M^5 dependency in the heating rate leads to a rapid increase resulting in a nearly complete depletion of the fuel at this point.

For points in the outer region which have a lower initial fuel density, the evolution is somewhat different. Radiation energy from the hotter central region passes through this outer region, however the parameters for this simulation limit the exchange of energy between radiation and material. The combination of a large diffusion loss rate and a poor coupling of radiation and material energy results in a lower material temperature. Due to the strong dependence of the reaction rate on temperature, T_M^5, the lower temperature outer region can have a significantly lower reaction rate. This results in incomplete consumption of fuel in this region.

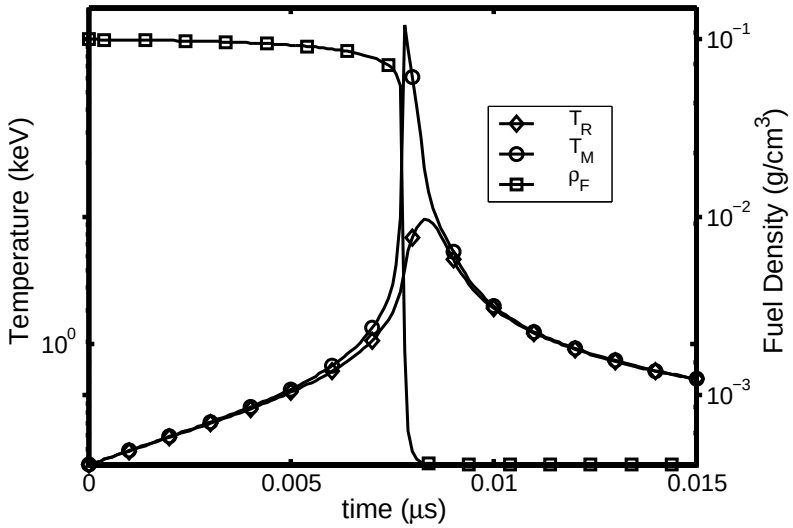

Fig. 6. Time dependence of radiation and material temperatures and fuel density at $x = 0, y = 0$.

Fig. 7 give contours of material temperature, radiation temperature and fuel density at $t = 0.0085\mu s$. At this time, the fuel has been significantly depleted in the central region. The material temperature is high around the inner edge of the remaining fuel and the central material temperature is held down by the transfer to the cooler radiation. The radiation is heated by the cylindrical shell-like region of high material temperature. This heating, along with diffusion, keeps the radiation temperature in the central region flat. Lastly, the shell-like region of unconsumed fuel is still present at the end of the simulation.

In order to study the convergence of this problem with respect to reducing the tolerance, we made several simulations varying RTOL from 10^{-7} to 10^{-10} for maximum orders of integration of 2 and 5. For this series of runs the numerical statistical counters and parameters defined by,

RTOL = relative tolerance,
MO = maximum order allowed,
NST = time steps,
NNI = nonlinear iterations,
NLI = linear iterations,
RT = run time in seconds,

are given in Table 2. Here we see a substantial decrease in the run times due to using a higher maximum integration order. The time stepping algorithm is able to use the higher integration order to meet accuracy requirements with larger time steps resulting in a faster overall runtime for a given accuracy

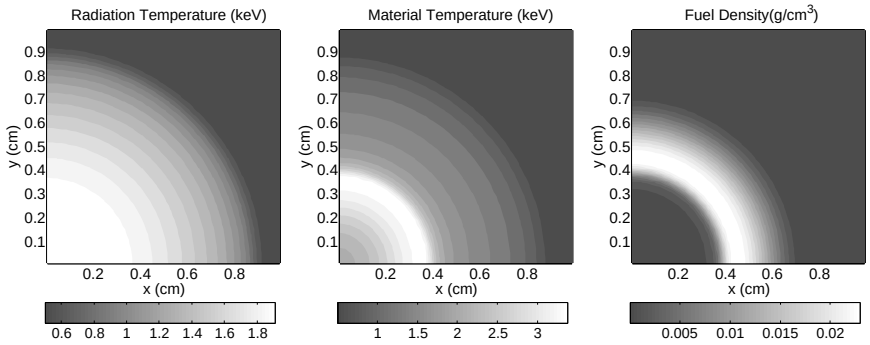

Fig. 7. Radiation temperature, material temperature and fuel density at $t = 0.0085\mu s$.

with the higher maximum integration order. This advantage is seen in savings for all integration statistics, including the cummulative numbers of linear and nonlinear iterations required for solution. Lastly, we again see a significant increase in run time to meet accuracy requirements for RTOL values below 10^{-9}.

Table 2. Statistics for 2D Fusion Fuel Problem

RTOL	MO	NST	NNI	NLI	RT (sec)
10^{-7}	2	17,384	20,807	62,322	1,730
10^{-7}	5	14,510	17,479	52,369	1,449
10^{-8}	2	45,768	56,333	136,973	4,152
10^{-8}	5	35,686	45,797	116,451	3,347
10^{-9}	2	113,545	140,788	292,722	9,313
10^{-9}	5	81,535	110,791	224,178	7,414
10^{-10}	2	266,722	323,349	621,406	20,564
10^{-10}	5	172,137	242,944	433,689	15,500

As a measure of accuracy for these runs, we determined the maximum relative error in material temperatures over the entire 2D grid. This quantity is shown in Fig. 8. The relative error is computed with respect to the most highly resolved run, $RTOL = 10^{-10}$, $MO = 5$. This plot indicates that the reduction in error is approximately linearly related to RTOL. Note that Fig. 8 also indicates that $MO = 5$ runs are more accurate than $MO = 2$ for the same RTOL. The relative error plots are all similar in that the maximum is during the sharp rise in material temperature. Relative error plots for the other components of the system, radiation temperature and fuel density, are similar and are thus not shown.

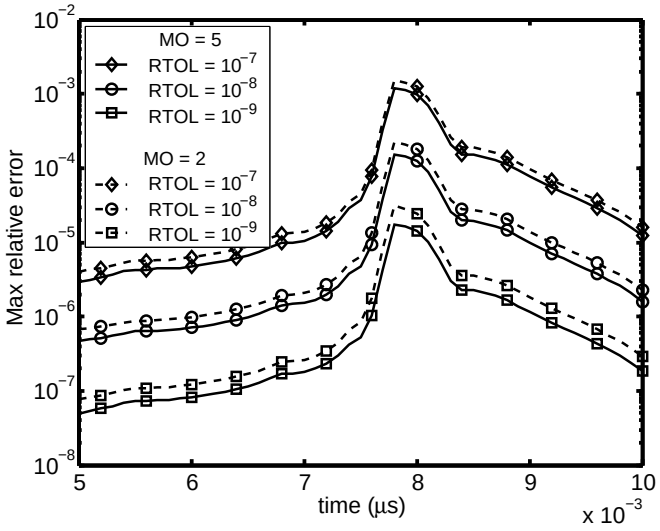

Fig. 8. Maximum relative error in material temperature vs time for maximum order, MO, 2 and 5

5 Conclusions

We have presented fully implicit solutions of a three equation system including: (1) radiation energy evolution with diffusion and exchange with material energy; (2) material energy evolution with reaction heating and exchange with radiation energy; and (3) fuel density evolution with depletion due to consumption. Our solution method makes use of high order in time integration methods, inexact Newton-Krylov nonlinear solvers, and multigrid preconditioning using a Schur complement strategy. We have demonstrated accurate solution of the fusion heating and fuel evolution by comparison with an analytic solution for a simplified problem. Using a 2D problem which encompasses all the processes included in our model, we have demonstrated convergence to a highly resolved result. As before [8], our test problems have shown that increasing the order of time integration leads to a more accurate and efficient method.

Acknowledgements

This work was performed under the auspices of the U. S. Dept. of Energy by University of California, Lawrence Livermore National Laboratory under contract W-7405-ENG-48.

References

1. A. J. Mewadows, Stellar Evolution, Pergamon Press, 1978, p. 97.
2. J. J. Duderstadt, G. A. Moses, Inertial Confinement Fusion, John Wiley and Sons, 1982, p. 131.
3. D. A. Knoll, W. J. Rider, G. L. Olson, Nonlinear convergence, accuracy, and time step control in nonequilibrium radiation diffusion, J. Quant. Spec. and Rad. Trans. 70 (1) (2001) 25–36.
4. V. A. Mousseau, D. A. Knoll, W. J. Rider, Physics-based preconditioning and the Newton–Krylov method for non-equilibrium radiation diffusion, J. of Comput. Phys. 160 (2000) 743–765.
5. D. J. Mavriplis, Multigrid approaches to non-linear diffusion problems on unstructured meshes, Num. Lin. Alg. with App. 8 (8) (2001) 499–512.
6. L. Stals, Comparison of non-linear solvers for the solution of radiation transport equations, Elec. Trans. Num. Anal. 15 (2003) 78–93.
7. P. N. Brown, C. S. Woodward, Preconditioning strategies for fully implicit radiation diffusion with material-energy transfer, SIAM J. Sci. Comput. 23 (2) (2001) 499–516.
8. P. N. Brown, D. E. Shumaker, C. S. Woodward, Fully implicit solution of large-scale non-equilibrium radiation diffusion with high order time integration, J. Comp. Phys. 204 (2) (2005) 760–783.
9. D. L. Ropp, J. N. Shadid, C. C. Ober, Studies of the accuracy of time integration methods for reaction-diffusion equations, J. Comp. Phys. 194 (2004) 544–574.
10. C. C. Ober, J. N. Shadid, Studies on the accuracy of time integration methods for the radiation-diffusion equations, J. Comp. Phys. 195 (2004) 743–772.
11. G. C. Pomraning, The Equations of Radiation Hydrodynamics, Pergamon, New York, 1973.
12. R. L. Bowers, J. R. Wilson, Numerical Modeling in Applied Physics and Astrophysics, Jones and Bartlett, Boston, 1991.
13. E. M. Corey, D. A. Young, A new prototype equation of state data library, Tech. Rep. UCRL-JC-127698, Lawrence Livermore National Laboratory, Livermore, CA, submitted to American Physical Society Meeting (1997).
14. J. Wesson, Tokamaks, Clarendon Press, Oxford, 2004, p. 13.
15. D. J. Rose, J. Melville Clark, Plasmas and Controlled Fusion, M.I.T. Press, 1961, p. 322.
16. T. J. Dolan, Fusion Research Vol. 1, Principles, Pergamon Press, 1980, p. 29.
17. G. D. Byrne, A. C. Hindmarsh, PVODE, an ODE solver for parallel computers, Int. J. High Perf. Comput. Appl. 13 (1999) 354–365.
18. A. C. Hindmarsh, P. N. Brown, K. E. Grant, S. L. Lee, R. Serban, D. E. Shumaker, C. S. Woodward, SUNDIALS: Suite of nonlinear and differential/algebraic equation solvers, ACM Trans. Math. Soft.To appear. Also available as Lawrence Livermore National Laboratory Technical Report UCRL-JP-200037.
19. P. N. Brown, G. D. Byrne, A. C. Hindmarsh, VODE: A variable-coefficient ODE solver, SIAM J. Sci. Stat. Comput. 10 (5) (1989) 1038–1051.
20. K. R. Jackson, R. Sacks-Davis, An alternative implementation of variable step-size multistep formulas for stiff ODEs, ACM Trans. Math. Software 6 (1980) 295–318.

21. Y. Saad, M. H. Schultz, GMRES: A generalized minimal residual algorithm for solving nonsymmetric linear systems, SIAM J. Sci. Stat. Comput. 7 (3) (1986) 856–869.
22. S. F. Ashby, R. D. Falgout, A parallel multigrid preconditioned conjugate gradient algorithm for groundwater flow simulations, Nuclear Science and Engineering 124 (1) (1996) 145–159.
23. S. Schaffer, A semi-coarsening multigrid method for elliptic partial differential equations with highly discontinuous and anisotropic coefficients, SIAM J. Sci. Comp. 20 (1) (1998) 228–242.
24. P. N. Brown, R. D. Falgout, J. E. Jones, Semicoarsening multigrid on distributed memory machines, SIAM J. Sci. Stat. Comput. 21 (5) (2000) 1823–1834.
25. J. E. Jones, C. S. Woodward, Newton-Krylov-multigrid solvers for large-scale, highly heterogeneous, variably saturated flow problems, Advances in Water Resources 24 (2001) 763–774.
26. W. F. Briggs, V. E. Henson, S. F. McCormick, A Multigrid Tutorial, 2nd. Edition, SIAM, Philadelphia, PA, 2000.